communications chemistry

A Nature Portfolio journal

Article

https://doi.org/10.1038/s42004-026-02119-y

Subsonic phase front propagation in martensitic transitions of 1,2,4,5-tetrabromobenzene single crystals

Check for updates

Ken Takazawa ✉ & Jun-ichi Inoue

Martensitic transitions in organic crystals, which are diffusionless structural phase transitions between polymorphs, are topics of current interest. These transitions proceed by fast propagation of the phase front (phase boundary) across the crystals and induce fascinating phenomena, such as thermosalient effect and superelasticity, which have potential applications in molecular devices. Revealing the mechanism of these transitions is of crucial importance for understanding the origins of these phenomena and for their device applications. To this end, here we observe the spatio-temporal evolution of the phase front in temperature-induced martensitic transition in 1,2,4,5-tetrabromobenezen (TBB) crystals. We observed subsonic phase front propagation across the crystals with the velocity of up to ~800 m/s. The analysis using a nonlinear lattice model based on Landau's theory of phase transitions showed that the phase front motion is described as a propagating solitary wave in a non-conservative system. Our results revealed the essential factors governing organic martensitic transitions and novel insights into the transition mechanism.

Structural phase transitions between polymorphs of organic crystals induced by external stimuli, such as temperature and pressure, have attracted increasing attention. These transitions give rise to fascinating phenomena, such as the thermosalient effect, superelasticity, and shape memory effect, which have potential applications in organic crystal-based devices[1–32]. Crystallographic, thermodynamic, and spectroscopic investigations of these phase transitions have demonstrated that they are first-order diffusionless transitions that proceed with small, albeit cooperative, motion of the constituent molecules. Therefore, they are referred to as organic martensitic transitions by analogy with martensitic transitions in Fe alloys[33,34]. The progression of the martensitic transition is characterized by nucleation followed by the propagation of the interface between the new and original phases (the phase front). This is in contrast to transitions accompanied by diffusive atomic/molecular motions, which proceed with the nucleation of multiple small domains followed by the growth of these domains (the nucleation and growth mechanisms).

Although numerous studies on martensitic transitions in metals and alloys have been performed for many years, their organic counterparts are emerging research areas, and the mechanisms of the transitions are topics of ongoing research. A promising approach to gain crucial information for understanding the mechanisms is direct and real-time observation of the phase front propagation. The velocity, propagation direction with respect to the crystallographic axes, and width of the phase front are closely related to the thermodynamic and elastic properties of the crystal as well as to the packing and interactions of molecules in the crystal. All these properties together govern the dynamics of phase transitions. Therefore, the detailed analysis of phase front dynamics by employing an appropriate theoretical model reveals the essential factors governing the phase transitions.

However, phase front propagation has been directly observed for only a few organic martensitic crystals to date[13–15,21] because of the following experimental difficulties: for most martensitic transitions, the new phase cannot be clearly distinguished from the original phase with standard optical measurements. Because the molecular structure of individual molecules remains nearly unchanged throughout the transition, the color and/or optical density of the new phase is also almost the same as that of the original phase. In addition, the martensitic transition is generally a fast process and is often accompanied by an explosive crystal motion, such as jumping and sudden cracking (the thermosalient effect)[1–8,10–19]. Therefore, to observe phase front propagation, a measurement technique with a high time resolution is required. For this reason, the phase front propagation has been successfully observed only for non-thermosalient crystals so far[13–15,21].

Here, we developed a technique for acquiring an image of a crystal during a martensitic phase transition, where the new and original phases are clearly distinguished. By combining this technique with an ultrahigh-speed camera, we observed the phase front propagation in single crystals of 1,2,4,5-tetrabromobenzene (TBB, Fig. 1a). A TBB crystal is a typical thermosalient crystal, which exhibits martensitic transition accompanied by an explosive crystal motion[1,35]. We observed ballistic phase front propagation from one

Research Center for Electronic and Optical Materials, National Institute for Materials Science, Tsukuba, Japan. ✉e-mail: takazawa.ken@nims.go.jp

edge to the other across a single crystal of TBB. The velocity of the phase front reached ~800 m/s, which is 5–6 orders of magnitude higher than those previously reported for martensitic transitions of non-thermosalient crystals. The measured velocities were up to ~60% of the sound velocity (phonon velocity) in the TBB crystals, i.e., phase front propagation was subsonic. This finding indicates that the observed phenomena are not adequately described by linear elastic wave models. To account for the subsonic propagation, we employed a one-dimensional nonlinear lattice model that explicitly takes into account the fact that the transition between the two phases is first-order. We demonstrate that our model quantitatively explains the subsonic phase-front propagation in TBB crystals and reveal novel insights into the mechanism of the organic martensitic transitions.

Results

TBB single crystals

A single crystal of TBB was reported to transform from β- to γ-phase near room temperature, around 40 °C upon heating[1,35–37]. The crystal structures of both the β- and γ-phases belong to a monoclinic system with the space group $P2_1/n$. The lattice parameters are $a = 10.2355(5)$ Å, $b = 10.7193(4)$ Å, $c = 4.0233(2)$ Å, $\beta = 100.184(5)°$, $V = 434.47(4)$ Å^3, and $Z = 2$ for the β-phase at $T = 30$ °C, whereas they are $a = 9.8719(5)$ Å, $b = 11.0780(5)$ Å, $c = 4.0549(3)$ Å, $\beta = 100.585(5)°$, $V = 435.90(4)$ Å^3, and $Z = 2$ for the γ-phase at $T = 40$ °C[37]. As shown in Fig. 1b, c, the distortion of the unit cell through the $\beta \rightarrow \gamma$ transition is anisotropic, i.e., it expands along the b- and c-axes and shrinks along the a-axis. The anisotropic cell distortion is a common

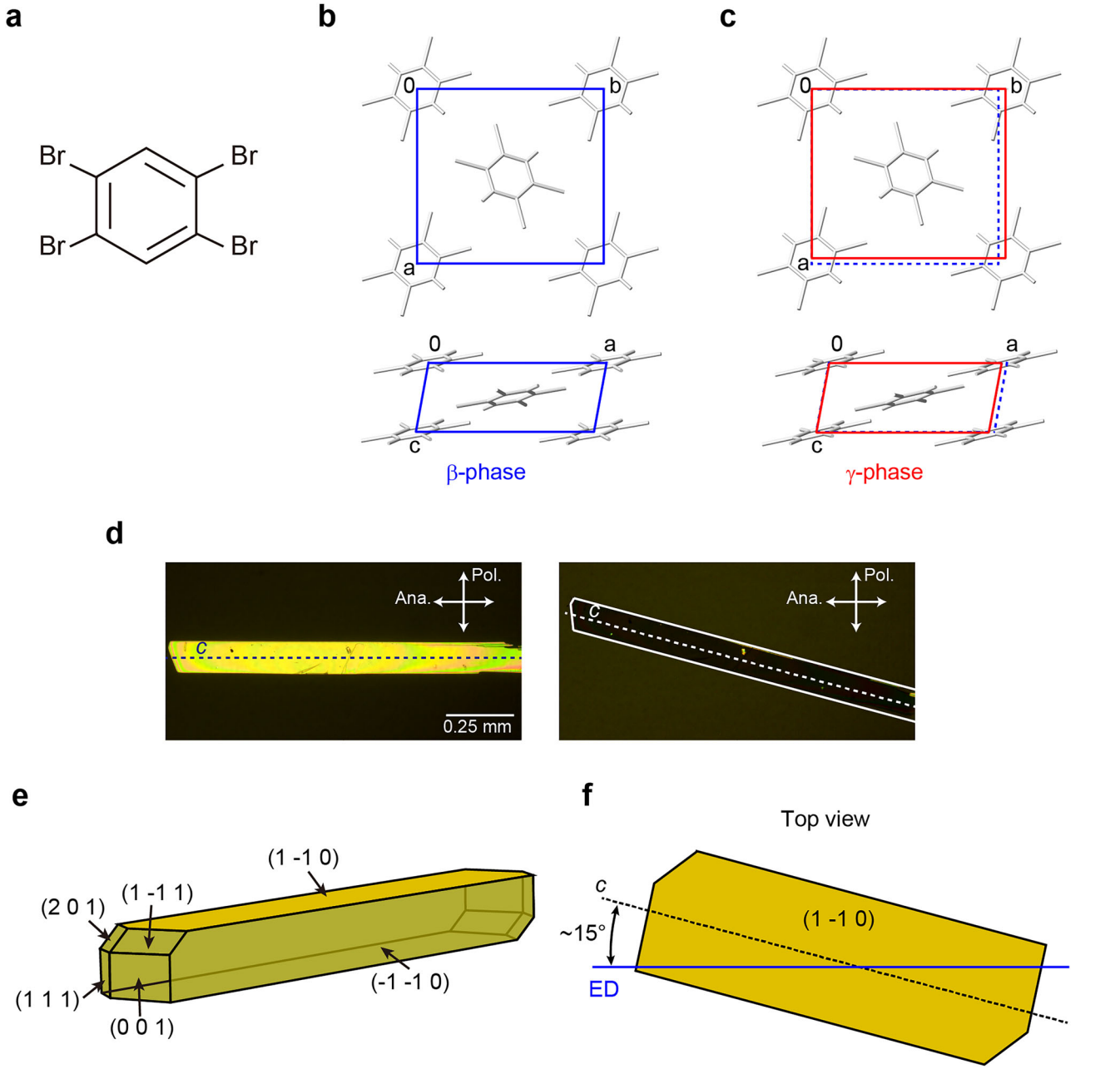


Fig. 1 | Structure and morphology of TBB single crystals. a Chemical structure of TBB. Crystal structures of **b** β-phase and **c** γ-phase. Dashed blue lines show the unit cell of β-phase. **d** Left panel: crossed-polarized microscope image of a TBB crystal oriented so that the c-axis is parallel to the analyzer. The arrows indicate directions of the polarizer and the analyzer. Right panel: image of the crystal at the extinction direction. **e** Crystal faces of a TBB single crystal. **f** Top view of a crystal. The extinction direction (ED) is shown by the blue line.

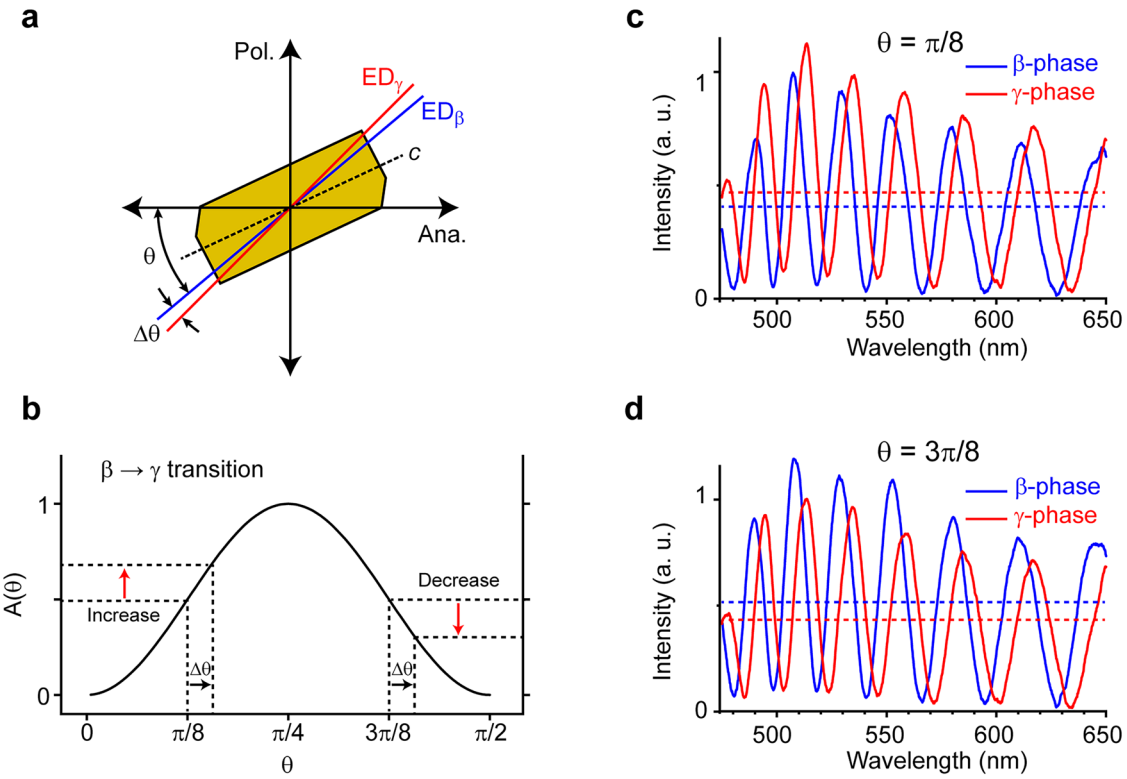


Fig. 2 | Effect of phase transition on the polarization properties of a TBB crystal. **a** Rotation of ED by the phase transition. ED_β and ED_γ show the extinction direction of the β- and γ-crystal, respectively. **b** Curve of $A(\theta)$. Red arrows indicate increase and decrease in $A(\theta)$ at $\theta = \pi/8$ and $3\pi/8$, respectively, through the $\beta \rightarrow \gamma$ transition. **c** Transmission spectra of a TBB crystal oriented at $\theta = \pi/8$ before (blue curve) and after (red curve) the $\beta \rightarrow \gamma$ transition. Averaged spectral intensities are indicated by dashed lines. **d** Same as (**c**) at $\theta = 3\pi/8$.

characteristic of organic martensitic phase transitions[33]. The changes in the lattice constants are −3.55%, +3.35%, and +0.79% along the *a*-, *b*-, and *c*-axes, respectively, whereas that in the unit cell volume is only +0.33% owing to the anisotropy. A crystal in the γ-phase transforms back to the β-phase upon cooling at ~35 °C. The temperature hysteresis of ~5 °C between the $\beta \rightarrow \gamma$ and $\gamma \rightarrow \beta$ transitions indicates that the transition is first-order.

TBB crystals were grown via slow evaporation from a saturated ethanol solution. The crystals had an elongated plate-like shape with a length along the long axis of up to ~5 mm and a thickness of a few hundred micrometers (Fig. 1d). The crystal faces were identified based on previously reported assignments[38] and Bravais–Friedel–Donnay–Harke simulations (Fig. 1e)[39]. The primary crystal plane is (1 −1 0) and contains the crystallographic *c*-axis (Fig. 1f). Using a cross-polarized light microscope, the extinction direction was observed to decline by ~15° with respect to the *c*-axis, as previously reported (Fig. 1f and right panel of Fig. 1d)[38].

Effect of phase transitions on polarization properties

The β-crystals were heated from room temperature across the phase transition temperature (~40 °C) under a polarized light microscope. We observed that the extinction direction slightly rotated upon the $\beta \rightarrow \gamma$ transition. The rotation angle ($\Delta\theta$) was measured for 15 crystals and determined to be $\Delta\theta = 1.55°$ ($s = 0.43$). In the following section, we demonstrate that this rotation can be used to observe the spatio-temporal evolutions of the phase transition.

The spectrum of light transmitted through a crystal under a cross-polarized microscope is given by

$$I(\theta, \lambda) \propto \sin^2(2\theta) \cdot \sin^2\left(\frac{\pi R}{\lambda}\right) = A(\theta) \cdot B(\lambda) \quad (1)$$

where θ is the angle between the extinction direction of the crystal and the polarization direction of the analyzer (Fig. 2a), R is the retardation expressed as $R = d\Delta n$, where d is the crystal thickness, and Δn is the birefringence[40]. Because $|dA(\theta)/d\theta|$ is maximum at $\theta = \pi/8$ and $3\pi/8$, $A(\theta)$ most sensitively changes with $\Delta\theta$ at these crystal orientations (Fig. 2b). For a positive $\Delta\theta$, $A(\theta)$ increases and decreases at $\theta = \pi/8$ and $3\pi/8$, respectively. We measured $I(\theta, \lambda)$ of the TBB crystal at these orientations before and after the phase transition. The blue curve in Fig. 2c shows $I(\theta = \pi/8, \lambda)$ measured at 23 °C, where the crystal is in the β-phase. The spectrum exhibits several fringes attributed to $B(\lambda)$ in Eq. 1. The total intensity of the transmitted light was evaluated by averaging $I(\theta = \pi/8, \lambda)$ over the spectral range and is indicated by the blue dashed line in the Fig. 2c. Subsequently, the crystal was heated above the transition temperature (~40 °C), and $I(\theta = \pi/8, \lambda)$ was measured after it transformed to the γ-phase (the red curve). The fringes shifted slightly with respect to those of the β-phase, indicating that $B(\lambda)$ was affected by the transition. The average intensity of the spectrum is indicated by the red dashed line. It was determined that the intensity increased by ~11% upon the $\beta \rightarrow \gamma$ phase transition. A similar measurement was performed at $\theta = 3\pi/8$ (Fig. 2d). At this orientation, the transmitted light intensity decreased by ~12% through the $\beta \rightarrow \gamma$ transitions. These changes in intensity are sufficiently large to distinguish between the β- and γ-phases when the crystal is recorded using a video camera during the phase transition.

We further examined the effect of phase transition on both $A(\theta)$ and $B(\lambda)$. We observed that the extinction direction rotated by $\Delta\theta \approx 1.55°$ upon phase transition. Using Eq. 1, the change in $A(\theta)$ induced by this rotation ($[A(\theta + \Delta\theta) - A(\theta)]/A(\theta)$) is calculated as 0.11 and −0.11 at $\theta = \pi/8$ and $3\pi/8$, respectively. These values approximately agree with the observed changes in the intensities of the transmitted light, i.e., ~11% and ~−12% at $\theta = \pi/8$ and $3\pi/8$, respectively. This agreement implies that the changes were mostly attributable to those in $A(\theta)$. Because $B(\lambda)$ provides multiple fringes in the spectra and the phase transition induces a small shift of them, the change in the averaged $B(\theta)$ over the spectral range is small. The TBB crystals investigated in this study all satisfied the conditions, where the change in $B(\lambda)$ was

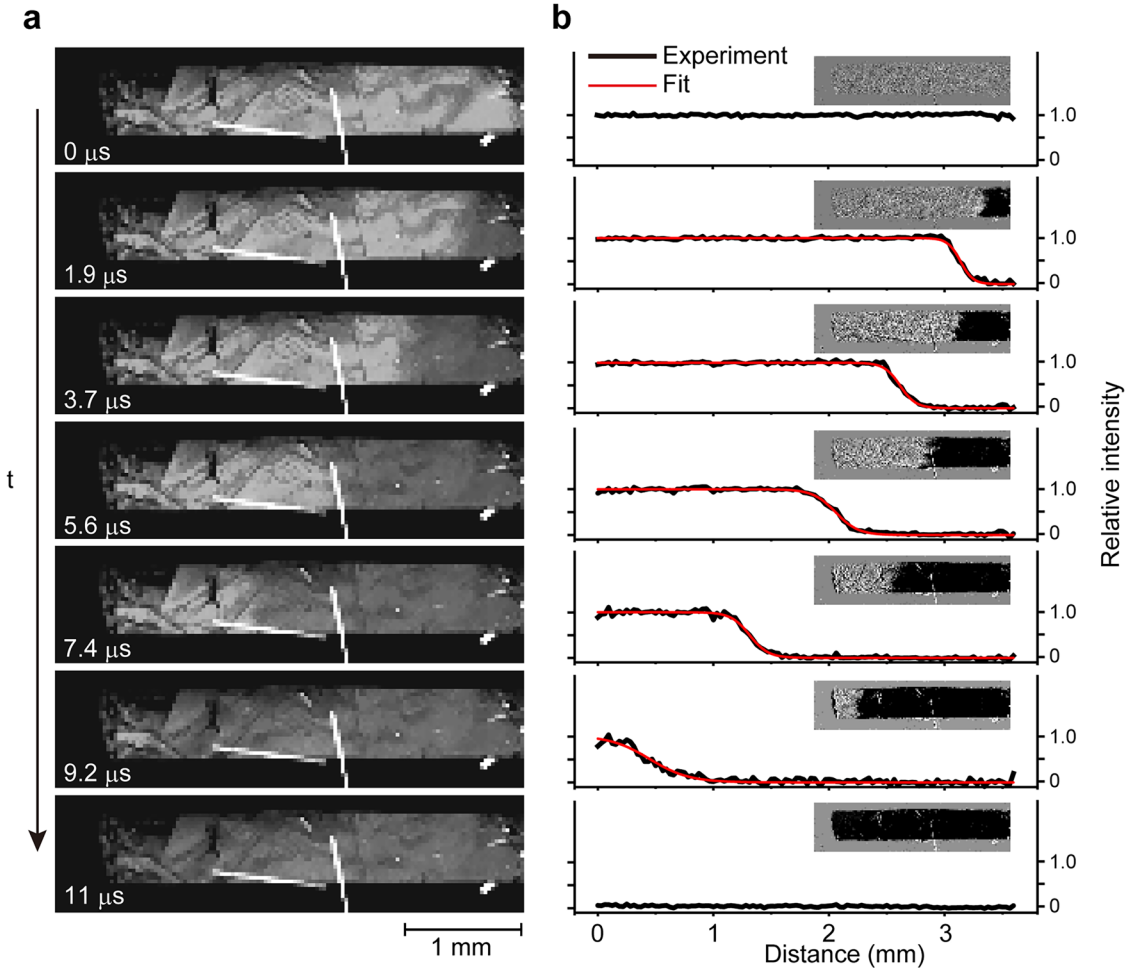


Fig. 3 | Phase front propagation in the phase transition of a TBB crystal recorded with the high-speed camera. a Snapshots recorded during the phase transition. **b** Black curves: intensities of the transmitted light obtained by integrating the crystal images along the vertical axis of the snapshots. Red curves: fitted curves using the sigmoid function. Insets: images obtained by subtracting those recorded 10 μs before the phase transition.

negligible for the transmitted light intensity. A detailed analysis of the effect of phase transition on $B(\lambda)$ is provided in the Supplementary Information.

Direct observation of phase front propagation

We demonstrated that the β- and γ-phases can be distinguished by orienting the crystals at specific angles. Based on this result, we recorded videos of the TBB crystals during the phase transition using a high-speed camera. Figure 3a shows snapshots of a TBB crystal with height and width of 0.6 and 3.6 mm, respectively, recorded by the camera operated at 5.4×10^5 fps with the exposure time for each frame of 1/3,811,764 s (≈262 ns) during the $\gamma \rightarrow \beta$ transition (see also Supplementary Video 1). The crystal was oriented at $\theta = \pi/8$. The dark region, which corresponds to the β-phase, appeared at the right edge of the crystal and extended toward the left edge of the crystal with maintaining the clear boundary between the dark and bright regions (the phase front). The difference in intensity between the bright and dark regions was approximately 10%, which was consistent with the above analysis. These images clearly indicate that the phase transition proceeds by phase front propagation.

To measure the position of the phase front in each snapshot precisely, the image captured ~10 μs before the phase transition was subtracted from those recorded during the phase transition (insets in Fig. 3b). This procedure eliminates the inhomogeneity of the transmitted light that is unrelated to the phase transition and allows for a clear visualization of the phase front. Then, the intensity of the image was integrated along the vertical axis and plotted as a function of the horizontal position of the crystal (black curves in Fig. 3b). The positions of the phase fronts were determined by fitting a sigmoid function to the curves (red curves in Fig. 3b). The velocity of the phase front (v_{pf}) was then evaluated from the difference of the phase front positions between those in two adjacent frames as $v_{pf} = 5.4 \times 10^5 \ (x_{n+1} - x_n)$ m/s, where x_n is the position of the phase front in the nth frame (note that $n = 1$ represents the frame, where the phase front was first captured). The evaluated v_{pf} values for this crystal were plotted against n in the right panel of Fig. 4 (red squares) and were 300–450 m/s. The sigmoid curves in Fig. 3b show that the width of the transition region varies for each snapshot. The width can be affected by many factors, such as the tilt angle of the (0 0 1) plane with respect to the substrate, the movement of the phase front during the exposure time of the camera, and the slight tilt of the phase front with respect to the long axis of the crystal. At present, it is not clear which factors determine the width.

We performed these measurements and analyses for ~30 crystals with lengths along the [0 0 1] direction ranging from 0.8 to 4.2 mm for both $\beta \rightarrow \gamma$ and $\gamma \rightarrow \beta$ transitions. The transition temperatures were 38 ± 1.5 and 35 ± 1.5 °C for the $\beta \rightarrow \gamma$ and $\gamma \rightarrow \beta$ transitions, respectively. Videos of some of them are provided in the Supplementary Video 2. The following features were observed for all the crystals: (1) the phase transition started at one of the short edges, and the phase front propagated along the [0 0 1] direction; (2) phase front was perpendicular to the [0 0 1] direction; and (3) when the phase transition started from one edge in the $\beta \rightarrow \gamma$ transition induced by heating, it started from the other in the $\gamma \rightarrow \beta$ transition induced by subsequent cooling.

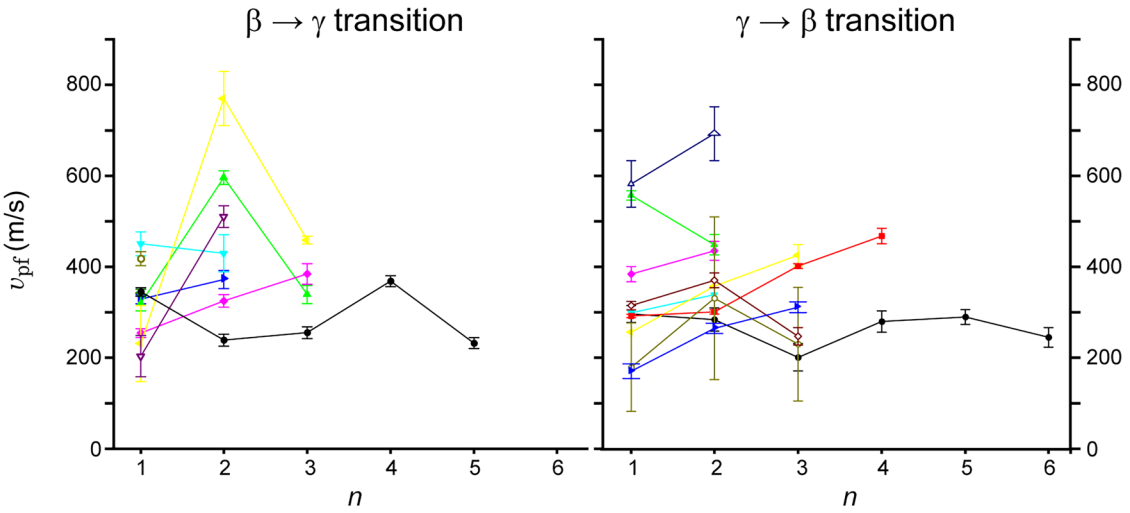


Fig. 4 | Velocity of the phase front (v_{pf}). Left panel: the $\beta \rightarrow \gamma$ transition. Right panel: the $\gamma \rightarrow \beta$ transition. The v_{pf} values obtained from the same crystal are shown by the same symbol and color in the left and right panels. The v_{pf} values were obtained using the relation $v_{pf} = 5.4 \times 10^5 (x_{n+1} - x_n)$ m/s, where x_n is the position of the phase front in the nth frame. The x_n values were determined by fitting sigmoid functions to the data points (see the text and Fig. 3b). The number of data points (N) is different for each crystal depending on its size (N = 118 (◀), 120 (▲), 85 (▽), 77 (▼), 65 (◁), 97 (♦), 81 (▶), 125 (●), 102 (○), 76 (△), 111 (◇), 104 (▪)). The error bars were evaluated from the standard errors of x_n, which were obtained by the sigmoidal fitting.

The v_{pf} values were plotted in the left (the $\beta \rightarrow \gamma$ transitions) and right (the $\gamma \rightarrow \beta$ transitions) panels of Fig. 4. For a large crystal, the phase front was captured over several frames before the entire crystal was transformed, providing several data points on the graph, whereas a small crystal provided few data points. Therefore, the number of data points is related to the crystal size. For crystals smaller than ~0.8 mm, the phase front was captured only in one frame or not captured at all. Thus, v_{pf} for such small crystals could not be evaluated. The graph shows that v_{pf} ranges 200–800 m/s for both the $\beta \rightarrow \gamma$ and $\gamma \rightarrow \beta$ transitions, and no clear correlation between v_{pf} and the crystal size was found. We do not have enough data on the correlation between v_{pf} and a crystal thickness. However, we observed a tendency that larger crystals have larger thicknesses. Therefore, the absence of correlation between v_{pf} and the crystal size suggests that v_{pf} does not correlate with the thickness. Because the crystals were heated by thermal contact with the substrate, a temperature gradient along the thickness of the crystals may exist and affect v_{pf}. However, the absence of a correlation between v_{pf} and the thickness further suggests that the effect of the temperature gradient on v_{pf} is minimal.

The fluctuations of v_{pf} with n observed for some crystals may be attributed to the inhomogeneity of crystal quality. The v_{pf} values and their fluctuations are not reproducible. The phase front motions could be observed repeatedly over several heating/cooling cycles for the same crystal. However, the repeated phase transitions caused gradual destruction (cracking and disintegration) of the crystal, leading to low v_{pf} and large fluctuations. Therefore, the v_{fp} values presented in Fig. 4 were all measured for the first heating/cooling cycles.

The fact that the phase front is perpendicular to the [0 0 1] direction suggests that the molecular motions in the (0 0 1) sheet are significantly faster than those in the [0 0 1] direction. Dye et al. studied the anharmonicity of molecular interactions in a TBB crystal in the β-phase and showed that the barrier for molecular motions in the *ab* plane is lower than that along the *c*-axis, supporting faster motions in the (0 0 1) sheet[41]. This indicates that the molecular motions in the (0 0 1) sheet are cooperative and that the phase transition proceeds in a sheet-by-sheet (layer-by-layer) manner (Fig. 5a), as observed for other organic martensitic transitions[21,22,42,43]. On the other hand, if the cooperative motions occur in the (0 1 0) or (1 0 0) sheets, phase-front propagation should be observed along the width of the crystal (Fig. 5b). This is clearly inconsistent with our observations. This layer-by-layer progression of the phase transition allows us to model a TBB crystal as a one-dimensional chain of interacting masses, which represent the (0 0 1) sheets (Fig. 5c). A theoretical analysis of phase front propagation based on this model is provided in a later section.

We observed that the phase transition always started not in the middle but at one of the short edges of the crystals. This is likely attributed to an instability of the edges due to surface free energy. We also observed that when the phase transition started at one of the short edges in the $\beta \rightarrow \gamma$ transition by heating, it started at the other short edge in the $\beta \rightarrow \gamma$ transition by subsequent cooling. This feature is also understood in terms of the surface free energy. The surface free energy of both edges are, to a greater or lesser extent, different, and the $\beta \rightarrow \gamma$ transition started from the edge with the higher energy when the crystal is heated. Upon the phase transition, the energies of both edges lowered. However, the edge with the higher energy in the β-phase should be more stabilized than the others. As a consequence, when the crystal is subsequently cooled, the $\gamma \rightarrow \beta$ transition started at the other edge, which has the higher energy in the γ-phase.

To investigate the mechanism behind the significantly fast phase front propagation, we compare the v_{pf} values with the sound velocity (phonon velocity) in TBB crystals. The anisotropic sound velocities of a TBB single crystal in the β-phase were investigated using Brillouin light scattering[41,44]. Based on the elastic constants provided in ref. 41, the sound velocities in the [0 0 1] direction were calculated as v_L = 2146 m/s, v_{TA1} = 1283 m/s, and v_{TA2} = 1469 m/s, where v_L and $v_{TA1,\ 2}$ are the longitudinal and transverse velocities, respectively (Supplementary Information). Therefore, the observed v_{pf} value of 800 m/s are approximately 40% and 60% of the longitudinal and transverse sound velocities, respectively, indicating that the phase front propagation in the TBB crystals is subsonic.

The v_{pf} values previously measured for martensitic, but non-thermosalient crystals, were on the order of μm/s to mm/s[13,21], and therefore, 5–6 orders of magnitude smaller than those observed for TBB crystals. This suggests that the fast phase front propagation is a key factor in the occurrence of the thermosalient effect. The v_{pf} values of these non-thermosalient crystals were analyzed based on the change rates of the volume fractions of the two phases, which are governed by the free energy curve along the transition coordinate[45]. Yangui et al. successfully observed the phase front motion in the martensitic phase transition of organic-inorganic perovskite crystals ($v_{pf} \approx$ 1.6 mm/s)[46] and qualitatively analyzed the phase front propagation based on the change rates of the volume fractions[47].

The v_{pf} values as high as the sound velocity have been reported for inorganic crystals. Mariette et al. performed femtosecond time-resolved X-

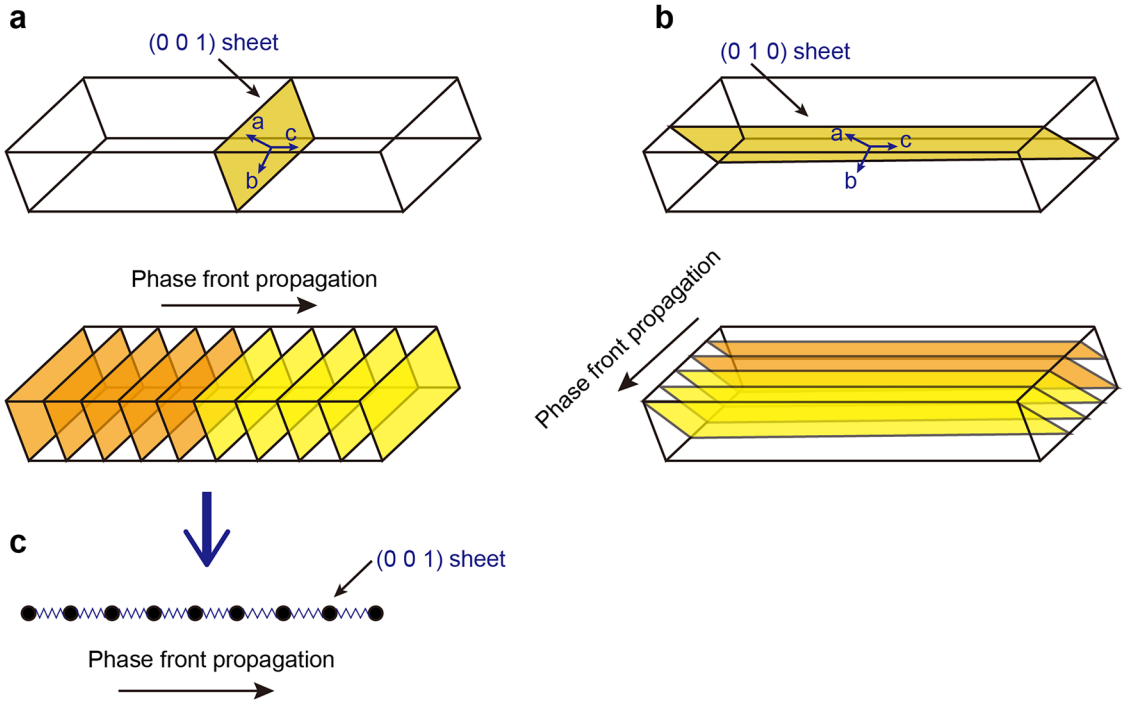


Fig. 5 | Layer-by-layer progression of the phase transition in TBB crystals. **a** Upper panel: the (0 0 1) sheet is indicated by the yellow plane. Lower panel: orange and yellow planes represent those in the new and original phases, respectively. The phase front propagates along the long axis of the crystal. **b** Upper panel: the (0 1 0) sheet is indicated by the yellow plane. Lower panel: orange and yellow planes represent those in the new and original phases, respectively. The phase front propagates along the short axis of the crystal. **c** 1D chain model, where masses (black circles) representing the (0 0 1) sheets are connected with springs.

ray powder diffraction measurements on Ti_3O_5 nanoparticles during a structural phase transition induced by a short-pulsed laser irradiation[48]. Detailed analysis of the diffraction data showed that the phase transition is triggered by the precursor photo-induced electronic changes accompanied by cell distortions and proceeds with the motion of the phase front with sound velocity ($v_{pf} \approx 6.5 \times 10^3$ m/s). To explain the phase front motion, they employed a one-dimensional model, where a strain wave (an acoustic wave) created by pulsed laser irradiation propagated across the crystal with the velocity of sound, leaving behind the new phase. They demonstrated that experimental observations were quantitatively reproduced using the strain wave model[49].

The v_{pf} values on the same order of magnitude as the sound velocity observed for the TBB crystals strongly suggest that the phase front propagation is also associated with the acoustic wave traveling across the crystal. However, the strain wave model is not applicable to TBB crystals because the v_{pf} values are considerably less than the sound velocity. The solutions of a linear wave equation, including strain waves, propagate with an exact sound velocity, in contrast to the subsonic v_{pf} of TBB crystals. Moreover, v_{pf} for the TBB crystals was observed to differ in the range 200–800 m/s depending on the crystal, suggesting that v_{pf} is sensitively influenced by small differences in the intrinsic and/or extrinsic properties of the individual crystals. This feature is hardly accounted for by the linear models. These observations led us to explore a suitable model for describing the phase front propagation in TBB crystals.

Analysis using a nonlinear lattice model

Here, we employ a one-dimensional nonlinear lattice model in accordance with Landau's phase transition theory. Landau's theory is based on free energy as a function of an order parameter. The free energy needs to be expanded up to sixth order for a first-order phase transition, whereas the fourth order for a second-order phase transition[50]. As stated earlier, the transition exhibited by the TBB crystals is of the first order, and the crystal can be modeled as a one-dimensional chain of coupled point masses that represent (0 0 1) sheets (Fig. 5c). Subsequently, a sixth-order on-site potential is incorporated into the mass chain model. Theoretical analyses of this type of model system, according to Lagrangian mechanics, have been conducted by several authors. We followed the work by Gooding et al.[51]. Using a dimensionless scalar order parameter $\phi(x, t)$ (x: position, t: time) that is detailed below, the on-site potential is written in the following form:

$$V_{\mathrm{on-site}}(\phi) = \frac{1}{2}\rho^* {\omega_0}^2 \left(\phi^2 - 1\right)^2 \left(\phi^2 + E_g\right) \tag{3}$$

where ρ^* is a parameter linearly related to the density ρ, ω_0 is the frequency, and E_g is a parameter that determines the potential profile ($0 < E_g < 1/2$)[51]. Our model, which consists of a harmonically coupled mass chain with the on-site potential, is schematically illustrated in Fig. 6a. The on-site potential has two stable equilibria at $\phi = \pm 1$, corresponding to the γ-phase, and a metastable equilibrium at $\phi = 0$ (the β-phase). In this model, the propagation of the phase front is viewed as a collective motion of the masses, where the displacement of a mass from $\phi = 0$ to 1 occurs consecutively from one site to the neighboring site. From a wave mechanics perspective, this collective motion is described as the propagation of a kink-like solitary wave with velocity v_{pf}. We sought such kink-like wave solutions for the model system.

Previous studies demonstrated that this system has propagating kink-like solutions with a constant v_{pf} only when the system is non-conservative[51–54]. Although v_{pf} fluctuated during the propagation (Fig. 4), we assume v_{pf} is constant throughout the transitions for simplicity. Subsequently, the Rayleigh dissipation function defined as $R = (1/2)\gamma(\phi_t)^2$ was introduced (hereafter, the italic subscripts denote differentiation). The field equation is derived from the Lagrangian density of the system, that is, $L = T - V$, where $T = (1/2)\rho^*(\phi_t)^2$ and $V = V_{\mathrm{on\text{-}site}} + (1/2)g(\phi_x)^2$, and is given by

$$\phi_{tt} = -{\omega_0}^2 \left[\left(1 - 2E_g\right)\phi + \left(2E_g - 4\right)\phi^3 + 3\phi^5\right] - \Gamma\phi_t + \frac{g}{\rho^*}\phi_{xx} \tag{4}$$

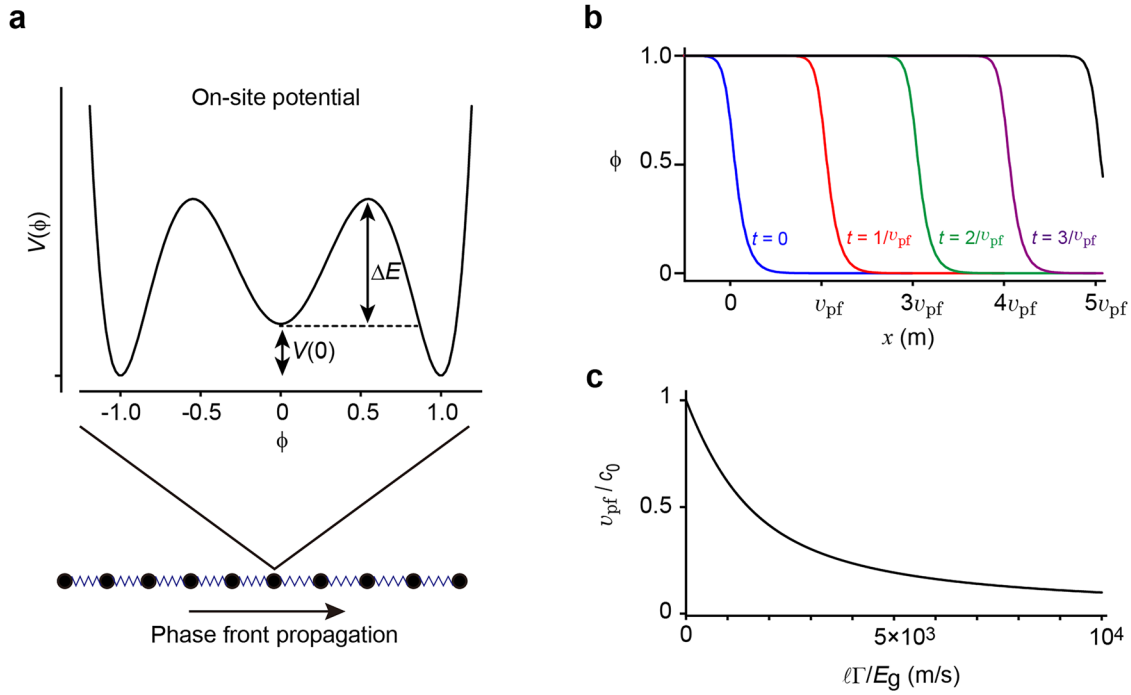


Fig. 6 | Analysis of the phase front propagation using the nonlinear lattice model. **a** 1D mass chain model with the on-site potential with nondegenerate minima. $V(0)$: energy difference between the metastable and stable minima. ΔE: barrier height. **b** Time evolution of the kink-like solution during the $\beta \rightarrow \gamma$ transition induced by heating. **c** The phase front velocity (v_{pf}/c_0) as a function of $\ell\Gamma/E_g$.

where $\Gamma = \gamma/\rho^*$ and g is the spring constant. The following dynamical kink-like solutions exactly satisfy the field equation:

$$\phi(x,t) = \left[1 + \exp\left(\frac{x - v_{pf}t}{\ell}\right)\right]^{-\frac{1}{2}} \quad (5)$$

with

$$\Gamma v_{pf} = 4{\omega_0}^2 E_g \ell \quad (6)$$

and

$$\ell^2 = \frac{g\Gamma^2}{\rho*}\left[4{\omega_0}^2\left(\Gamma^2 + 4{\omega_0}^2 {E_g}^2\right)\right]^{-1} \quad (7)$$

where ℓ is the width of the kink[51].

Figure 6b shows the time evolution of $\phi(x,t)$, showing that the γ-phase extends into the β-phase via propagation of their boundary with the constant velocity v_{pf}. Using Eqs. 5–7, v_{pf} is a monotonically decreasing function of $\ell\Gamma/E_g$, as

$$v_{pf} = -\frac{1}{2}\left(\frac{\ell\Gamma}{E_g}\right) + \sqrt{\frac{1}{4}\left(\frac{\ell\Gamma}{E_g}\right)^2 + {c_0}^2} < c_0 \quad (8)$$

where $c_0 = (g/\rho^*)^{1/2}$ is the sound velocity (Fig. 6c). The parameter $\Gamma\,(=\gamma/\rho^*)$ characterizes the dissipation of the system, which likely differs for each crystal depending on intrinsic factors, such as crystal quality and extrinsic factors, such as the adhesion between the crystals and the substrates. Therefore, $\ell\Gamma/E_g$ can differ for each crystal, resulting in a different v_{pf}. These results indicate that the model qualitatively captures the characteristic features of the phase front propagation associated with the phase transition of TBB crystals. It should be noted that in an actual crystal, the molecules in the (0 0 1) sheet at the phase front deflect both in and out of the (0 0 1) plane upon the phase transition (see Fig. 5a). Therefore, the phase front as a propagating wave has a mixed longitudinal-transverse character. In contrast, in the one-dimensional model, the phase front propagates as a pure longitudinal wave because the molecular motions are reduced to one-dimensional displacements of the point masses.

Quantitative validation of the nonlinear lattice model

Having confirmed the consistency of the model, next, we quantitatively analyzed the phase transition of the TBB crystal using the model. For quantitative analysis, the dimensionless order parameter ϕ must be converted into a quantity with the dimension of length. In the ϕ-space, the displacement between the metastable and stable equilibria is unity ($\phi = 0$–1). In an actual crystal, on the other hand, the displacement of the (0 0 1) sheets induced by the phase transition is given by the difference in the lattice constant c between the β- and γ-phases (Δc). Considering this correspondence, it is reasonable to scale $\phi = 1$ by Δc (=4.0549–4.0233 Å = 0.0316 Å). Using this conversion relation, and the previously reported thermal analysis data, including $V(0) = 330$ J/mol (the enthalpy of the phase transition[1,55]), and $\Delta E = 2000$ J/mol (the barrier height for the transformation[37,56]), E_g is uniquely determined as $E_g = 2.2 \times 10^{-2}$ from Eqs. 5 to 7 (see Supplementary Information). The obtained on-site potential curve is shown in Fig. 7a.

Further, using this E_g value and the sound velocity c_0 in Eq. 8, we can explicitly evaluate all the other parameters (γ, ℓ, and ω_0) from Eqs. 5 to 7. As described earlier, in the one-dimensional model, collective motions of molecules in all three directions (the [1 0 0], [0 1 0], and [0 0 1] directions), which give rise to the fast longitudinal and slow transverse waves, are reduced to the displacement of the masses along the propagation direction. Therefore, c_0 does not need to agree with either the longitudinal and transverse sound velocities and can take a value between them ($v_L \geq c_0 \geq v_{TL1,\,2}$). Considering this point, we calculated the parameters for the high and low limiting c_0 values, namely, $c_0 = v_L$ and v_{T1}. For both the c_0 values, the parameters were consistently and uniquely determined for a given v_{pf} value (Supplementary Information) and those for $v_{pf} = 200$, 400, 600, and 800 m/s are listed in Table 1.

To assess the validity of this analysis, we compared these results with the experimental data. In our model, γ determines energy dissipation in the

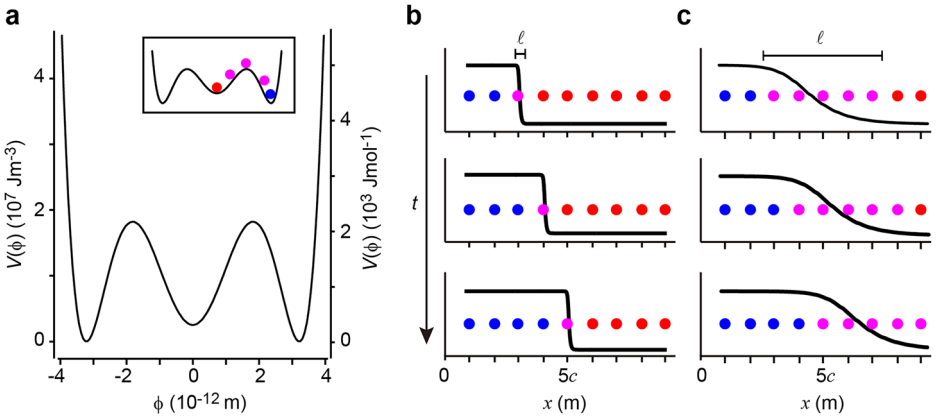


Fig. 7 | On-site potential and kink-like solutions obtained by the theoretical analysis. a On-site potential. **b** Time evolution of the kink-like solution (from top to bottom) for $\ell < c$. The color of a mass at each site represents displacement. The masses at the metastable and stable minima are shown in red and blue, respectively, whereas those at intermediate between them are shown in purple (see the inset in **a**). **c** The same as (**b**) for $\ell > c$.

Table 1 | Calculated parameters (γ, ℓ, and $\omega_0\gamma$) for v_{pf} = 200, 400, 600, and 800 m/s

v_{pf} (m/s)	γ (10^{-7} Ns/m^2)		l (10^{-12} m)		$\omega_0\gamma$ (10^7 N/m^2)	
	v_L	v_{TA1}	v_L	v_{TA1}	v_L	v_{TA1}
200	12.7	7.56	12.6	7.46	10.8	6.42
400	6.29	3.64	12.4	7.17	5.34	3.09
600	4.10	2.25	12.1	6.67	3.48	1.91
800	2.97	1.50	11.7	5.90	2.52	1.27

The sound velocities of v_L = 2146 m/s and v_{TA1} = 1283 m/s were used.

system. The corresponding quantity for the actual crystals is the viscosity (damping), which is given by the imaginary part of the complex Young's modulus, expressed as $E^* = E' + i\omega E''$ (E': Young's modulus, ω: frequency). Danno et al. measured the E^* values of several aromatic molecular crystals, such as triphenylene, 1,2,3,4-dibenzanthracene, and coronene, using forced resonance vibration methods and showed that the $\omega E''$ values of these crystals are all on the order of 10^7–10^8 N/m^2[57]. The $\omega_0\gamma$ values calculated from our analysis are listed in Table 1. For both the limiting values of $c_0 = v_L$ and v_{TA1}, they are on the order of 10^7 N/m^2, showing good agreement with the $\omega E''$ values of the aromatic crystals. This agreement strongly supports the validity of our analysis. The relationship between v_{pf} and γ values in Table 1 may suggest that variation in v_{pf} is attributed to that of γ, which can be influenced by the intrinsic and/or extrinsic properties of individual crystals. However, experimental measurements of the elastic properties of the crystals are required to verify this assumption.

Further support for the validity of the analysis is provided by examining the kink width ℓ. The evaluated ℓ is on the order of 10^{-12} m (Table 1). This is two orders of magnitude smaller than the lattice constant c and on the same order as the difference in the lattice constant c between the β- and γ-phases ($\Delta c = 3.16 \times 10^{-12}$ m), implying that the kink is always localized at a single site, as schematically illustrated in Fig. 7b. This indicates that the phase transition proceeds in a layer-by-layer manner, as expected from our experimental observations and the martensitic phase transitions of other organic crystals[20,33]. If ℓ is sufficiently large to extend over multiple sites, those within the kink width have intermediate displacements between the stable and metastable equilibria (Fig. 7c). This corresponds to the situation where there extends a region with intermediate crystal structures at the phase boundary, and is inconsistent with the layer-by-layer progression of the phase transition.

Discussion

In this study, we investigated the martensitic phase transitions in single crystals of TBB and observed that the transitions proceeded with the subsonic phase front propagation across the crystals. We demonstrated that the nonlinear lattice model successfully explained the motion of the phase front. The analysis reveals that the phase front is described as a kink-like solitary wave, which can be formed and propagate in a non-conservative system. This indicates that the viscosity of the crystals is the crucial factor in the formation and propagation of the phase front. A number of organic martensitic crystals, including thermosalient crystals, have been discovered to date, and studies aimed at device applications of these crystals have been extensively conducted. Our results serve as a promising guideline for analyzing and understanding the phase transitions of these crystals and provide valuable information for their device applications.

Methods

Sample preparation

TBB was obtained from Wako Pure Chemical Industries and purified by recrystallization from ethanol. A saturated ethanol solution of TBB was filtered using a syringe filter with 200 nm pores and then placed in a container with a lid with holes. After the crystals were grown via slow evaporation, they were washed with ethanol and dried under ambient conditions. Microscopic observations showed that approximately half of the crystals were twinned, and only non-twinned single crystals were used for the measurements.

Optical measurement

A TBB crystal was placed on a microscope cover glass (18 mm × 18 mm) and immobilized with a small amount of mineral oil to prevent movement of the crystal at the moment of phase transition. Although we attempted to perform the measurements on crystals that were simply placed on the cover glass without immobilization, most of them hopped or broke upon the phase transitions. We could observe phase front propagation for only a few crystals that did not exhibit movement. The v_{pf} values of these crystals were observed as ~600 m/s, suggesting that the immobilization does not largely affect v_{pf}. The sample was then placed on a transparent thermoplate (Tokai Hit). The thermoplate was mounted on the rotational stage of a polarized light microscope (Olympus, BX51-P) equipped with a modified illumination system. A 1.25 times objective lens was used. Because the exposure time for each frame in the high-speed camera recording was short (~262 ns), high-intensity illumination was required to capture images of the crystal. We constructed an illumination unit consisting of a 100 W mercury lamp and attached it to the microscope.

High-speed videos were recorded using a high-speed camera (Photron, FASTCAM) mounted on the microscope. A video of a crystal was loop-recorded while the sample temperature was varied at ~1 °C/min. When the crystal was transformed, the loop recording was immediately stopped so that the last ~3 s of the video was saved. Because the relative orientation between the stage and the camera is fixed, we can confirm that the crystals did not rotate upon the phase transitions by reviewing the videos. This ensures that the movement of the boundary between the dark and bright regions of the crystals is solely attributed to the change in the crystal structure.

Reporting summary

Further information on research design is available in the Nature Portfolio Reporting Summary linked to this article.

Data availability

The data that support the findings of this study are available from the corresponding author upon reasonable request.

Received: 17 November 2025; Accepted: 25 June 2026;
Published online: 07 July 2026

References

1. Lieberman, H. F., Davey, R. J. & Newsham, D. M. T. Br···Br and Br···H interactions in action: polymorphism, hopping, and twinning in 1,2,4,5 tetrabromobenzene. *Chem. Mater.* **12**, 490–494 (2000).
2. Ding, J., Herbst, R., Praefcke, K., Kohne, B. & Saenger, W. A crystal that hops in phase transition, the structure of trans, trans, anti, trans, trans-perhydropyrene. *Acta Cryst.* **B47**, 739–742 (1991).
3. Centore, R. et al. A series of compounds forming polar crystals and showing single-crystal-to-single-crystal transitions between polar phases. *CrystEngComm* **14**, 2645–2653 (2012).
4. Skoko, Z., Zamir, S., Naumov, P. & Bernstein, J. The thermosalient phenomenon. "Jumping crystals" and crystal chemistry of the anticholinergic agent oxitropium bromide. *J. Am. Chem. Soc.* **132**, 14191–14202 (2010).
5. Sahoo, S. C., Panda, M. K., Nath, N. K. & Naumov, P. Biomimetic crystalline actuators: structure–kinematic aspects of the self-actuation and motility of thermosalient crystals. *J. Am. Chem. Soc.* **135**, 12241–12251 (2013).
6. Panda, M. K. et al. Colossal positive and negative thermal expansion and thermosalient effect in a pentamorphic organometallic martensite. *Nat. Commun.* **5**, 4811 (2014).
7. Panda, M. K., Runčevski, T., Husain, A., Dinnebier, R. E. & Naumov, P. Perpetually self-propelling chiral single crystals. *J. Am. Chem. Soc.* **137**, 1895–1902 (2015).
8. Naumov, P., Chizhik, S., Panda, M. K., Nath, N. K. & Boldyreva, E. Mechanically responsive molecular crystals. *Chem. Rev.* **115**, 12440–12490 (2015).
9. Karothu, D. P., Weston, J., Desta, I. T. & Naumov, P. Shape-memory and self-healing effects in mechanosalient molecular crystals. *J. Am. Chem. Soc.* **138**, 13298–13306 (2016).
10. Khalil, A., Ahmed, E. & Naumov, P. Metal-coated thermosalient crystals as electrical fuses. *Chem. Commun.* **53**, 8470–8473 (2017).
11. Tamboli, M. I., Karothu, D. P., Shashidhar, M. S., Gonnade, R. G. & Naumov, P. Effect of crystal packing on the thermosalient effect of the pincer-type diester naphthalene-2,3-diyl-bis (4-fluorobenzoate): a new class II thermosalient solid. *Chem. Eur. J.* **24**, 4133–4139 (2018).
12. Ahmed, E., Karothu, D. P., Warren, M. & Naumov, P. Shape-memory effects in molecular crystals. *Nat. Commun.* **10**, 3723 (2019).
13. Li, L. et al. Martensitic organic crystals as soft actuators. *Chem. Sci.* **10**, 7327–7332 (2019).
14. Khalil, A., Karothu, D. P. & Naumov, P. Direct quantification of rapid and efficient single-stroke actuation by a martensitic transition in a thermosalient crystal. *J. Am. Chem. Soc.* **141**, 3371–3375 (2019).
15. Ahmed, E. et al. Ultrafast, light, soft martensitic materials. *Adv. Funct. Mater.* **32**, 2112117 (2022).
16. Colin-Molina, A. et al. Thermosalient amphidynamic molecular machines: motion at the molecular and macroscopic scales. *Matter* **1**, 1033–1046 (2019).
17. Omoto, K. et al. Thermosalience in macrocycle-based soft crystals via anisotropic deformation of disilanyl architecture. *J. Am. Chem. Soc.* **142**, 12651–12657 (2020).
18. Vušak, D., Naumov, P., Jelčić, Ž, Matković-Čalogović, D. & Prugovečki, B. Thermally induced reversible martensitic phase transition and self-healing in nickel glycinamide crystals. *Angew. Chem. Int. Ed.* **64**, e202421769 (2025).
19. Duan, Y. et al. Robust thermoelastic microactuator based on an organic molecular crystal. *Nat. Commun.* **10**, 4573 (2019).
20. Diao, Y. et al. Understanding polymorphism in organic semiconductor thin films through nanoconfinement. *J. Am. Chem. Soc.* **136**, 17046–17057 (2014).
21. Chung, H. et al. Rotator side chains trigger cooperative transition for shape and function memory effect in organic semiconductors. *Nat. Commun.* **9**, 278 (2018).
22. Chung, H., Ruzié, C., Geerts, Y. & Diao, Y. Hybrid mechanism of nucleation and cooperative propagation in a single-crystal-to-single-crystal transition of a molecular crystal. *Cryst. Growth Des.* **18**, 4245–4251 (2018).
23. Chung, H. et al. Single atom substitution alters the polymorphic transition mechanism in organic electronic crystals. *Chem. Mater.* **31**, 9115–9126 (2019).
24. Chung, H. et al. Understanding the role of bulky side chains on polymorphism of BTBT-based organic semiconductors. *Cryst. Growth Des.* **20**, 1646–1654 (2020).
25. Yao, Z. S. et al. Molecular motor-driven abrupt anisotropic shape change in a single crystal of a Ni complex. *Nat. Chem.* **6**, 1079–1083 (2014).
26. Brandel, C. et al. Mechanisms of reversible phase transitions in molecular crystals: case of ciclopirox. *Chem. Mater.* **27**, 6360–6373 (2015).
27. Takamizawa, S. & Miyamoto, Y. Superelastic organic crystals. *Angew. Chem. Int. Ed.* **53**, 6970–6973 (2014).
28. Takamizawa, S. & Takasaki, Y. Shape-memory effect in an organosuperelastic crystal. *Chem. Sci.* **7**, 1527–1534 (2016).
29. Mutai, T. et al. A superelastochromic crystal. *Nat. Commun.* **11**, 1824 (2020).
30. Borbone, F. et al. High-temperature reversible martensitic transition in an excited-state intramolecular proton transfer fluorophore. *Cryst. Growth Des.* **19**, 6519–6526 (2019).
31. Takazawa, K. et al. Phase-transition-induced jumping, bending, and wriggling of single crystal nanofibers of coronene. *Sci. Rep*. **11**, 3175 (2021).
32. Takazawa, K., Inoue, J. I. & Matsushita, Y. Repeatable actuations of organic single crystal fibers driven by thermosalient-phase-transition-induced buckling. *Small* **18**, 2204500 (2022).
33. Park, S. K. & Diao, Y. Martensitic transition in molecular crystals for dynamic functional materials. *Chem. Soc. Rev.* **49**, 8287–8314 (2020).
34. Reddy, C. M., Krishna, G. R. & Ghosh, S. Mechanical properties of molecular crystals—applications to crystal engineering. *CrystEngComm* **12**, 2296–2314 (2010).
35. Sahoo, S. C. et al. Kinematic and mechanical profile of the self-actuation of thermosalient crystal twins of 1,2,4,5-tetrabromobenzene: a molecular crystalline analogue of a bimetallic strip. *J. Am. Chem. Soc.* **135**, 13843–13850 (2013).
36. Johnson, F. B. Phase-change in 1,2,4,5-tetrabromobenzene investigated by pure quadrupole resonance. *Nature* **178**, 590–590 (1956).
37. Zakharov, B. A., Michalchuk, A. A., Morrison, C. A. & Boldyreva, E. V. Anisotropic lattice softening near the structural phase transition in the thermosalient crystal 1,2,4,5-tetrabromobenzene. *Phys. Chem. Chem. Phys.* **20**, 8523–8532 (2018).
38. White, K. M. & Eckhardt, C. J. Assignment of the Raman active lattice vibrations in various phases of 1,2,4,5-tetrabromobenzene and 1,2,4,5-tetrachlorobenzene crystals. *J. Chem. Phys* **90**, 4709–4718 (1989).
39. Docherty, R., Clydesdale, G., Roberts, K. J. & Bennema, P. Application of Bravais-Friedel-Donnay-Harker, attachment energy and Ising models to predicting and understanding the morphology of molecular crystals. *J. Phys. D* **24**, 89–99 (1991).

40. Bloss, F. D. An Introduction to the Methods of Optical Crystallography (Holt, Rinehart and Winston, 1961).
41. Dye, R. C. & Eckhardt, C. J. Semiempirical determination of intermolecular anharmonicity in molecular crystals: the case of 1,2,4,5-tetrabromobenzene. *J. Chem. Phys.* **91**, 3624–3630 (1989).
42. Anwar, J., Tuble, S. C. & Kendrick, J. Concerted molecular displacements in a thermally-induced solid-state transformation in crystals of DL-norleucine. *J. Am. Chem. Soc.* **129**, 2542–2547 (2007).
43. Zahn, D. & Anwar, J. Collective displacements in a molecular crystal polymorphic transformation. *RSC Adv.* **3**, 12810–12815 (2013).
44. Ko, J. H., Lee, K. S., Sahoo, S. C. & Naumov, P. Isomorphous phase transition of 1,2,4,5-tetrabromobenzene jumping crystals studied by Brillouin light scattering. *Solid State Commun.* **173**, 46–50 (2013).
45. Wollants, P., Roos, J. R. & Delaey, L. Thermally-and stress-induced thermoelastic martensitic transformations in the reference frame of equilibrium thermodynamics. *Prog. Mater. Sci.* **37**, 227–288 (1993).
46. Yangui, A. et al. Rapid and robust spatiotemporal dynamics of the first-order phase transition in crystals of the organic-inorganic perovskite $(C_{12}H_{25}NH_3)_2PbI_4$. *Sci. Rep.* **5**, 16634 (2015).
47. Slimani, A. et al. Velocity of the high-spin low-spin interface inside the thermal hysteresis loop of a spin-crossover crystal, via photothermal control of the interface motion. *Phys. Rev. Lett.* **110**, 087208 (2013).
48. Mariette, C. et al. Strain wave pathway to semiconductor-to-metal transition revealed by time-resolved X-ray powder diffraction. *Nat. Commun.* **12**, 1239 (2021).
49. Thomsen, C., Grahn, H. T., Maris, H. J. & Tauc, J. Surface generation and detection of phonons by picosecond light pulses. *Phys. Rev. B* **34**, 4129 (1986).
50. Fultz, B. *Phase Transitions in Materials* (Cambridge University Press, 2020).
51. Gooding, R. J. & Bales, G. S. Boosted kink-type solitary waves in nonlinear elastic media. *Phys. D* **55**, 251–258 (1992).
52. Gordon, A. & Genossar, J. Precursor order clusters at ferroelectric phase transitions. *Phys. B+C* **125**, 53–62 (1984).
53. Takeno, S. & Kisoda, K. Self-sustained kinks in a one-dimensional nonlinear lattice with dissipation. *J. Phys. Soc. Jpn.* **57**, 675–678 (1988).
54. González, J. A. & Holyst, J. A. Solitary waves in one-dimensional damped systems. *Phys. Rev. B* **35**, 3643–3646 (1987).
55. Mondieig, D., Cuevas-Diarte, M. A. & Haget, Y. Polymorphisme du tetrachloro-1,2,4,5 benzene et du tetrabromo-1,2,4,5 benzene. *J. Therm. Anal.* **35**, 2491–2500 (1989).
56. Zaczek, A. J., Catalano, L., Naumov, P. & Korter, T. M. Mapping the polymorphic transformation gateway vibration in crystalline 1,2,4,5-tetrabromobenzene. *Chem. Sci.* **10**, 1332–1341 (2019).
57. Danno, T., Kajiwara, T. & Inokuchi, H. Dynamic mechanical behaviour of organic molecular crystals. *I. Bull. Chem. Soc. Jpn.* **40**, 2793–2795 (1967).

Author contributions

K.T. performed the experiments and theoretical analyses. J.I. conducted the theoretical analyses. Both authors contributed to writing the manuscript.

Competing interests

The authors declare no competing interests.

Additional information

Supplementary information The online version contains Supplementary material available at https://doi.org/10.1038/s42004-026-02119-y.

Correspondence and requests for materials should be addressed to Ken Takazawa.

Peer review information *Communications Chemistry* thanks Céline Mariette, Panče Naumov and the other anonymous reviewer(s) for their contribution to the peer review of this work. A peer review file is available.

Reprints and permissions information is available at http://www.nature.com/reprints

Publisher's note Springer Nature remains neutral with regard to jurisdictional claims in published maps and institutional affiliations.

Open Access This article is licensed under a Creative Commons Attribution-NonCommercial-NoDerivatives 4.0 International License, which permits any non-commercial use, sharing, distribution and reproduction in any medium or format, as long as you give appropriate credit to the original author(s) and the source, provide a link to the Creative Commons licence, and indicate if you modified the licensed material. You do not have permission under this licence to share adapted material derived from this article or parts of it. The images or other third party material in this article are included in the article's Creative Commons licence, unless indicated otherwise in a credit line to the material. If material is not included in the article's Creative Commons licence and your intended use is not permitted by statutory regulation or exceeds the permitted use, you will need to obtain permission directly from the copyright holder. To view a copy of this licence, visit http://creativecommons.org/licenses/by-nc-nd/4.0/.

© The Author(s) 2026